A Model of Rocky Mountain Lee Cyclogenesis

PETER R. BANNON

Department of Meteorology, The Pennsylvania State University, University Park, Pennsylvania

(Manuscript received 16 January 1991, in final form 27 November 1991)

ABSTRACT

A quasi-geostrophic model of cyclogenesis in the lee of the Rocky Mountains treats the cyclogenesis as a forecasting problem and uses an initial value approach. The model consists of the interaction of a growing baroclinic wave with an infinitely long mountain ridge. This transient interaction simulates many of the observed features of the phenomena, including the formation of a lee trough concurrent with the poleward displacement of the incident low on the upstream side of the mountain and the development of a lee cyclone equatorward of the unperturbed storm track. Despite this development, the low is weakened by its interaction with the orography.

These results are explained physically and compared with those using a normal-mode approach to lee cyclogenesis.

1. Introduction

The Rocky Mountains of North America lie in a roughly north–south orientation and extend in an unbroken arc from Alaska to central Mexico. Isolated peaks reach 4–6 km in elevation with a mean height of 2–3 km. Their presence affects the weather and climate of the local region as well as that of the Northern Hemisphere as a whole. Petterssen (1956) first documented the climatological evidence for the formation of cyclones in the lee of the Rockies.

The synoptic structure of a lee cyclogenesis event has been described for the Rocky Mountains by a variety of authors (Hess and Wagner 1948; Newton 1956; McClain 1960; Carlson 1961; Hage 1961; Fawcett and Saylor 1965; Pierrehumbert 1986). Figure 1 summarizes the salient characteristics of the cyclogenesis. Initially (Fig. 1a) a surface anticyclone resides over the mountains with a low over the Pacific Ocean incident on the West Coast. As the high moves to the southeast (Fig. 1b), the Pacific low moves poleward along the mountains. A thermal trough develops in the lee despite the presence of negative vorticity advection aloft. The Pacific low "protrudes eastward in amoeba-like fashion" (Hess and Wagner 1948, p. 9). About 1 day after the initial time (Fig. 1c), a low appears in the lee of the Rockies located well to the south of the last windward location of the Pacific low. The lee cyclone briefly moves to the southeast (Fig. 1d) before turning northeastward to follow a normal development downstream of the mountain.

Corresponding author address: Dr. Peter R. Bannon, Department of Meteorology, Pennsylvania State University, 503 Walker Building, University Park, PA 16802.

Two important aspects of lee cyclogenesis emerge from this observational review. First, the westward phase tilt with height of the Pacific low and its antecedent high suggests that the primary disturbance may be interpreted as a growing synoptic wave disturbance whose interaction with the mountain leads to the secondary lee cyclogenesis. Indeed, Newton (1956, p. 530) in his case study emphasizes that "a cyclone would probably have formed eventually without help from orographic influences." Second, the amoeba-like movement of the surface low across the mountains makes it difficult to track the low accurately across the mountains and suggests that the climatological studies describing the leeside maximum in the location of cyclogenesis centers may arise in part from this difficulty.

The various theories of lee cyclogenesis can now be evaluated, keeping in mind the typical scenario described above. The superposition theory of Hayes et al. (1987) emphasizes the quasi- and semigeostrophic interaction of the mean flow with the mountain ridge. Such an interaction on the f plane produces an anticyclone over the mountain top with weak cyclonic lobes both upstream and downstream (e.g., Bannon and Zehnder 1989). A propagating cyclonic disturbance embedded in the mean flow would then tend to weaken as it moves over the mountain top, only to reappear stronger in the lee. However, the strength of the mountain anticyclone diminishes rapidly with increasing forward wind shear (Hayes et al. 1987; Bannon 1991) unless there are strong surface winds, a feature not yet correlated with lee cyclogenesis. It should be noted that leeside strengthening does not occur in the pressure field since the correct solution (Bannon and Zehnder 1989) for two-dimensional flow exhibits no leeside pressure trough. While such a trough is present

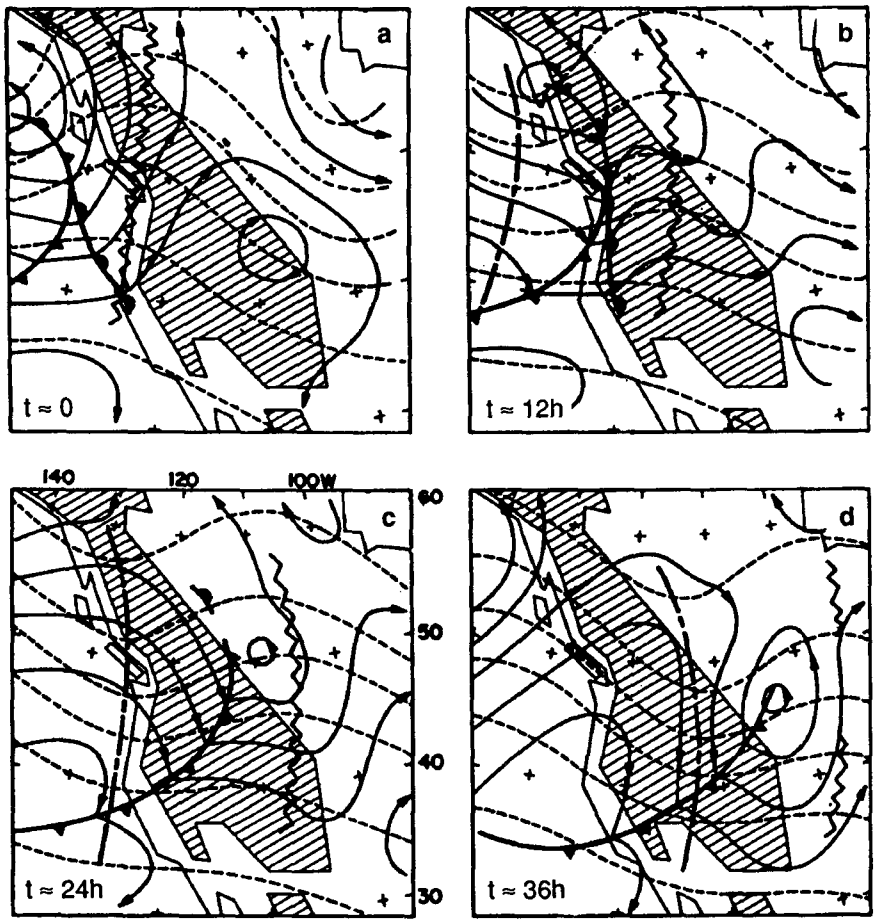

FIG. 1. Schematic model of Rocky Mountain lee cyclogenesis according to Palmén and Newton (1969). Panels (a)–(d) refer to the approximate times, t = 0, 12, 24, and 36 h, in the flow evolution. The shading represents a simplified orography with terrain higher than 1500 m. The heavy solid lines denote the surface fronts, the solid lines the 1000-mb contours, and the dashed lines the 500-mb contour. The upper trough line is dark-dotted; the ridge line is a zigzag pattern.

for steady solutions on the β plane, its large wavelength, $2\pi\sqrt{U/\beta} \approx 6\,000$ km, does not agree well with the scale of the lee cyclone.

Last, we note that the Hayes et al. model does not include the following observed features: the downstream displacement of the anticyclone initially over the mountain, the formation of an antecedent thermal trough, and the meridional displacement of the cyclone poleward upstream and equatorward downstream of the mountain.

The theory of Smith (1984, 1986) models lee cyclogenesis as the result of the orographic interaction of a steady flow exhibiting cold-air advection. This flow crudely represents the baroclinic zone of the parent cyclone with its upper-level trough. In an application to the Rockies, the model predicts a weak (~3 mb) lee trough after 12 hours of simulation. The questionable assumption of a static incident wind field severely restricts the validity of the model to a brief period late in the lee cyclogenesis scenario [e.g., panels (c) and (d) of Fig. 1]. Thus, it does not address such early signatures as the poleward displacement of the parent cyclone or the antecedent thermal troughing. Furthermore, the uniformity of the incident windfield restricts the applicability of the model to mountain ranges of relatively small horizontal extent.

An analogous theory by Clark (1990) emphasizes the role of the thermal troughing in the cyclogenesis. While not modeling its formation, Clark incorporates its effect on the surface wind field into the backshear model of Smith (1984). The results exhibit impressive deepening, but the same reservations as to the theory of Smith apply.

Buzzi et al. (1987) incorporate finite-amplitude topography into a two-layer model of baroclinic instability. The spatial structure of their most unstable mode agrees remarkably well with the observational scenario regarding the meridional displacement of the incident

and lee cyclones. They do not, however, address the mode's temporal character. The normal mode of Buzzi et al. (1990) has a similar spatial structure but travels too slowly (see their Fig. 12) compared with the observations summarized in Fig. 1. Typically (Buzzi and Speranza 1986), the orography has a stabilizing influence and reduces the growth rates of the unstable modes, which implies that the mountain has an upstream influence and alters the growth rate of the parent cyclone. Furthermore, the mode's growth rate is constant in time.

The purpose of the present study is to present a simple model of Rocky Mountain lee cyclogenesis as the transient interaction of a growing synoptic wave with a mountain ridge. As noted previously, the structure of the parent disturbance resembles that of a growing baroclinic wave (Eady 1949). Thus, the Eady model of baroclinic instability is altered to include an infinitely long mountain ridge aligned meridionally. Unlike Buzzi et al. (1987), we use an initial value approach and do not assume that the total topographic response is a normal mode with fixed temporal character. Thus, there is no far upstream influence by the mountain on the parent cyclone, and the growth rate can vary with time. The initial value and normal mode approaches are compared further in the conclusion.

We take the topographic forcing to be finite amplitude in the quasigeostrophic sense that the mountain height scaled by the fluid depth is the order of a Rossby number. This strong topography interacts only with the incident synoptic wave, which is assumed to be of small amplitude compared with the baroclinic unstable mean flow. This mean flow, however, is assumed to have zero surface wind, and thus there is no mean flow–mountain interaction.

The next section describes the details of the mathematical model and the techniques for its numerical solution. Section 3 presents the solution for a prototype calculation and discusses the essential physics of the simulation. Experiments addressing the sensitivity of the prototype results to the initial conditions and the model parameters are described in section 4.

2. The quasigeostrophic model

We assume that lee cyclogenesis is primarily a baroclinic phenomenon and that its essence can be captured using quasigeostrophic theory. The model atmosphere consists of an inviscid, Boussinesq fluid on an f plane with uniform basic-state buoyancy frequency N bounded above and below by rigid boundaries. The geostrophic streamfunction is

$$\psi = -(U_0 + U_z z)y + \phi(x, y, z, t), \qquad (2.1)$$

where U is the constant wind shear of the basic state. The constant surface wind U_0 is included here for convenience but will be dropped later in the analysis. Here ϕ is a small perturbation. The linearized potential vorticity equation is

$$\frac{d}{dt}\left(\nabla^2\phi + \frac{f^2}{N^2}\frac{\partial^2\phi}{\partial z^2}\right) = 0, \qquad (2.2)$$

where

$$\frac{d}{dt} = \frac{\partial}{\partial t} + (U_0 + U_z z)\frac{\partial}{\partial x}, \qquad (2.3)$$

and ∇^2 is the horizontal Laplacian operator. The associated thermodynamic equation for adiabatic flow is

$$\frac{d}{dt}\left(\frac{\partial\phi}{\partial z}\right) - U_z\frac{\partial\phi}{\partial x} + \frac{N^2}{f}w = 0. \qquad (2.4)$$

Note that the linearization of (2.2) and (2.4) involves ignoring terms quadratic in the perturbation streamfunction ϕ.

The vertical kinematic boundary conditions are

$$w = \left(U_0 - \frac{\partial\phi}{\partial y}\right)\frac{dh}{dx} \quad \text{at} \quad z = 0, \qquad (2.5)$$

and

$$w = 0 \quad \text{at} \quad z = H, \qquad (2.6)$$

where $H = 8$ km is the height of horizontal rigid-lid tropopause. The assumption of a lid is employed here to model the vertical gradient in potential vorticity from the troposphere to the stratosphere. Here

$$h(x) = \begin{cases} h_0 \cos^2(k_m x), & |k_m x| \leq \pi/2 \\ 0, & |k_m x| > \pi/2 \end{cases} \qquad (2.7)$$

is an idealized, infinitely long, ridge representation of the Rocky Mountains with height h_0. The choice of (2.7) rather than, say, a witch-of-Agnesi profile is predicated on the desire for a profile that is horizontally confined. For $k_m = 2\pi/(4000 \text{ km})$, the topography is nonzero within 10^3 km of the origin $x = 0$. Note that evaluation of (2.5) at $z = 0$ is a standard assumption of quasigeostrophic theory (Pedlosky 1987). Figure 2a summarizes the model physics and geometry.

Boundary condition (2.5) provides a convenient means to distinguish the present study from some earlier theories. Specifically, Hayes et al. (1987), Smith (1984, 1986), and Clark (1990) simplify (2.5) to

$$w = U_0\frac{dh}{dx} \quad \text{at} \quad z = 0. \qquad (2.8)$$

The cyclogenesis present in the latter two studies is therefore the result of the interaction of the mean incident flow with the topography. In the former study, (2.8) excites the stationary mountain anticyclone, which masks the propagating baroclinic disturbance. In the latter works, (2.8) generates a stationary lee trough for a backshear wind profile. Here we utilize (2.5) and allow the propagating disturbance (defined

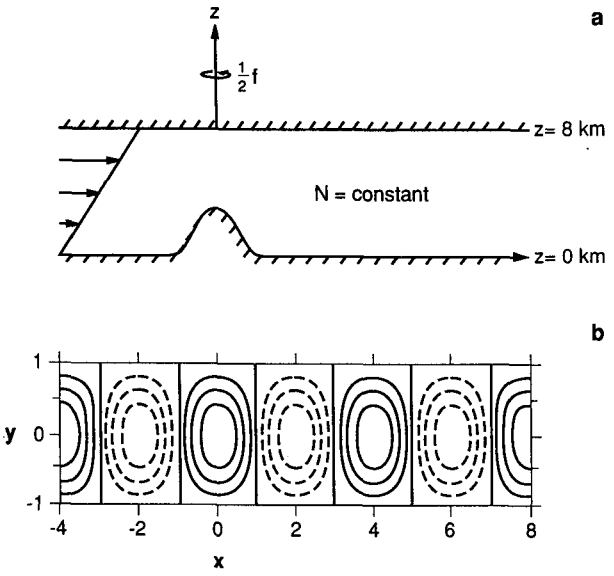

FIG. 2. (a) A zonal cross section of the numerical model. The model atmosphere is a uniformly stratified Boussinesq fluid of depth 8 km on an f plane. There is a cosine-squared mountain ridge of 3-km height along the origin $x = 0$. A small-amplitude baroclinic wave is growing on a mean flow with zero surface wind and a linear wind shear $U_z = 40$ m s^{-1} 10 km^{-1}. (b) A contour plot of the baroclinic wave at $t = 0$ for the basic experiment. The contour interval is one-fourth the maximum. Here and elsewhere the horizontal distances are in units of 1000 km, and dashed contours denote negative values.

below) to interact directly with the topography. Moreover, the mountain anticyclone is entirely suppressed by assuming that the mean surface wind vanishes:

$$U_0 = 0. \tag{2.9}$$

This assumption is consistent with the use of finite-amplitude quasigeostrophic topography.

Initially, we assume that a growing baroclinic wave exists near the topography. This initial condition reflects the discussion in the Introduction regarding the typical cyclogenesis scenario. Specifically we let the initial perturbation streamfunction be an Eady normal mode ϕ_E,

$$\phi(x, y, z, t = 0) = \phi_E(x, y, z, t = 0), \tag{2.10}$$

where

$$\phi_E = \mathrm{Re}\{\phi_0[\cosh\mu z + b \sinh\mu z]e^{ik(x-ct)} \cos ly\}, \tag{2.11}$$

with

$$b = -U_z/(\mu c), \quad \mu^2 = N^2(k^2 + l^2)/f^2 \tag{2.12}$$

and

$$c \equiv c_r + ic_i = U_z H\left\{\frac{1}{2} \pm \frac{1}{\mu H}\left[\left(\frac{\mu H}{2} - \coth\frac{\mu H}{2}\right) \times \left(\frac{\mu H}{2} - \tanh\frac{\mu H}{2}\right)\right]^{1/2}\right\}. \tag{2.13}$$

Figure 2b provides a contour plot of the surface pressure field associated with the initial condition (2.10) for a square wave ($k = l = 2\pi/4000$ km). An anticyclone lies over the mountain ridge with a cyclonic disturbance to the east. This situation is an idealization of Fig. 1a.

The cosinuous (i.e., cosly) dependence of (2.11) assures that the zonal wind of the disturbance is nonzero and that it will interact with the topography through the boundary condition (2.5). Note that this interaction will depend linearly on the disturbances meridional wavenumber l. Furthermore, inspection of (2.2), (2.4), and (2.5) indicates that this interaction excites a sinuous (i.e., sinly) response in the meridional direction. Thus, we assume a solution of the form

$$\phi(x, y, z, t) = \phi_c(x, z, t) \cos ly + \phi_s(x, z, t) \sin ly, \tag{2.14}$$

which represents the lowest-order mathematical representation of the wave–orography interaction. While it is common practice (e.g., Pedlosky 1987) to assume a channel geometry with meridional walls, this artificial approach is not adopted here.

The mathematical problem posed by (2.1)–(2.12) is solved numerically as an initial value one using standard finite difference techniques. The time marching scheme uses forward time differencing for the first step and a leapfrog thereafter. The time step is 30 min. To avoid mode splitting in the long term (36 day) integration discussed in section 5, a third-order Adams–Bashforth scheme is used in place of the leapfrog scheme. The difference between the two schemes is negligible for the short-term (4 day) integration reported in sections 3 and 4. The zonal domain is 12 000 km with periodic boundary conditions in x. The vertical domain is 8 km. The x–z spatial dependence is treated using centered differences with a 120 × 16 grid (i.e., resolution $\Delta x = 100$ km $\Delta z = 500$ m). The ϕ field is staggered in the vertical to handle the Neumann boundary condition implied by (2.4) to solve the elliptic component of (2.2) using successive overrelaxation (SOR). Verification of the numerical technique was achieved by integration of the control no-mountain experiment, which set the mountain height to zero, $h_0 = 0$. Excellent agreement with the growth rates given by the analytic expression (2.13) was obtained.

The next section describes in detail the results of a benchmark calculation and provides a qualitative explanation of the simulated phenomena. Section 4 summarizes the results of some sensitivity experiments.

3. Basic experiment

a. Numerical results

The numerical model was run for four simulated days with the initial condition of a growing Eady normal mode. This mode is a square wave ($k = l$) with a zonal wavelength of 4000 km. For the parameter values

of Table 1, $kNH/f = 1.26$, and the mode is close to the most unstable wave (Fig. 3) with an e-folding rate $\sigma = kc_i = 0.7$ day^{-1}. It propagates eastward at 16 m s^{-1} (Fig. 3) in the absence of a mountain. As Fig. 2 indicates, the wave is such that a surface pressure maximum lies exactly over the top of the mountain ridge at $x = 0$.

Figure 4 displays the subsequent time evolution of the surface pressure field at 6-h intervals over the first three days of simulation. The time sequence clearly reveals the following features

- The surface anticyclone originally over the mountain top moves to the southeast during the first day. It then gradually moves to the east-northeast, approaching its original latitude ($y = 0$).
- The surface cyclone immediately upstream of the mountain moves westward. Once encountering the mountain, it is deflected to the northeast. During the second day (panels e–h), the cyclone crosses the mountain to reappear at the start of the third day in the lee to the south of its original latitude. Its amoeba-like motion is clearly evident. After crossing the mountain, the cyclone travels an east-northeast path similar to the anticyclone that preceded it.
- A trough develops during the first day on the lee-side of the mountain in advance of the approaching cyclone. The trough recedes to the northeast as the cyclone traverses the mountain during day 2.

Figure 5a summarizes the movement of both the surface low and high during the simulation by plotting the position of the disturbance center (i.e., the extremum) every 3 hours. The loci of points for the low suggest a discontinuity in position from its mountain position to its location in the lee. Table 2 shows that this 800-km southward and 700-km eastward jump of the low center occurs essentially instantaneously in the model. It is conceivable that improvements in the temporal and spatial resolution of the numerical model (not attempted here) may enable the low center to be tracked continuously down the mountain slope. However, the synoptic implication of this discontinuous track is that *it appears as if a low first forms on the lee side without being traceable upstream.*

Figure 5 also documents the growth of the low pressure as it moves eastward. (Recall that the contour

TABLE 1. Parameter settings for the basic experiment.

Bouyancy frequency, N	10^{-2} s^{-1}
Coriolis parameter, f	10^{-4} s^{-1}
Mean wind shear, U_z	4×10^{-3} s^{-1}
Mean surface wind, U_0	0
Mountain height, h_0	3 km
Mountain wavelength, $2\pi/k_m$	4×10^3 km
Initial disturbance wavelength, $2\pi/k$	4×10^3 km
Disturbance meridional wavelength, $2\pi/l$	4×10^3 km

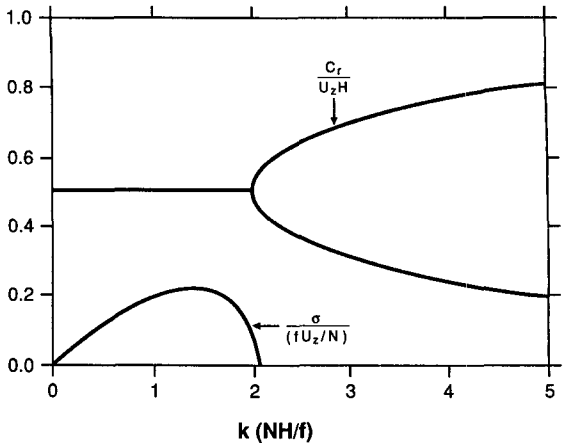

FIG. 3. The phase speed, c_r, and growth rate, $\sigma = kc_i$, of the Eady normal modes given by (2.13) for a meridional wavelength of 4000 km.

intervals in Fig. 4 are normalized by the maximum pressure anomaly at each time. In practice, the extremum corresponds to that of the undisturbed flow upstream of the mountain since, as shown below, the local influence of the mountain is cyclolytic.) The initial amplitude δp of the surface low is arbitrary in this study, and we take $\delta p = 2.5$ mb. Figure 5c shows that upon encountering the mountains the low deepens but at a reduced rate until it is near the mountaintop where it briefly fills. Note that the influence of the mountain is to produce a weaker lee low, which then undergoes enhanced growth before returning far downstream to a growth-rate characteristic of the low in the no-mountain control. A period of enhanced growth in the lee is a feature of alpine cyclogenesis (Buzzi and Tibaldi 1978). It is not known if this feature is also characteristic of Rocky Mountain cyclones.

The nature of the lee cyclogenesis in the midtroposphere is examined in Fig. 6, which plots the location and growth of the low pressure anomaly (i.e., trough) at 4 km associated with the surface low incident on the mountain. Figure 6a indicates that the evolution of the trough is similar to that of the low. However, the meridional excursions of the trough are smaller, and its movement over the mountain is more continuous. As the surface low decelerates ascending the mountain, the trough catches up to it. During this phase the growth of both the low and the trough is reduced. The subsequent discontinuous jump in the location of the surface low signals a period of enhanced growth of both features while they are more widely separated.

b. Discussion

A simple vorticity argument (Newton 1956; Carlson 1991) adequately explains most of the features of the model simulation. Figure 7 provides a schematic of this argument. In regions of ascending flow over the

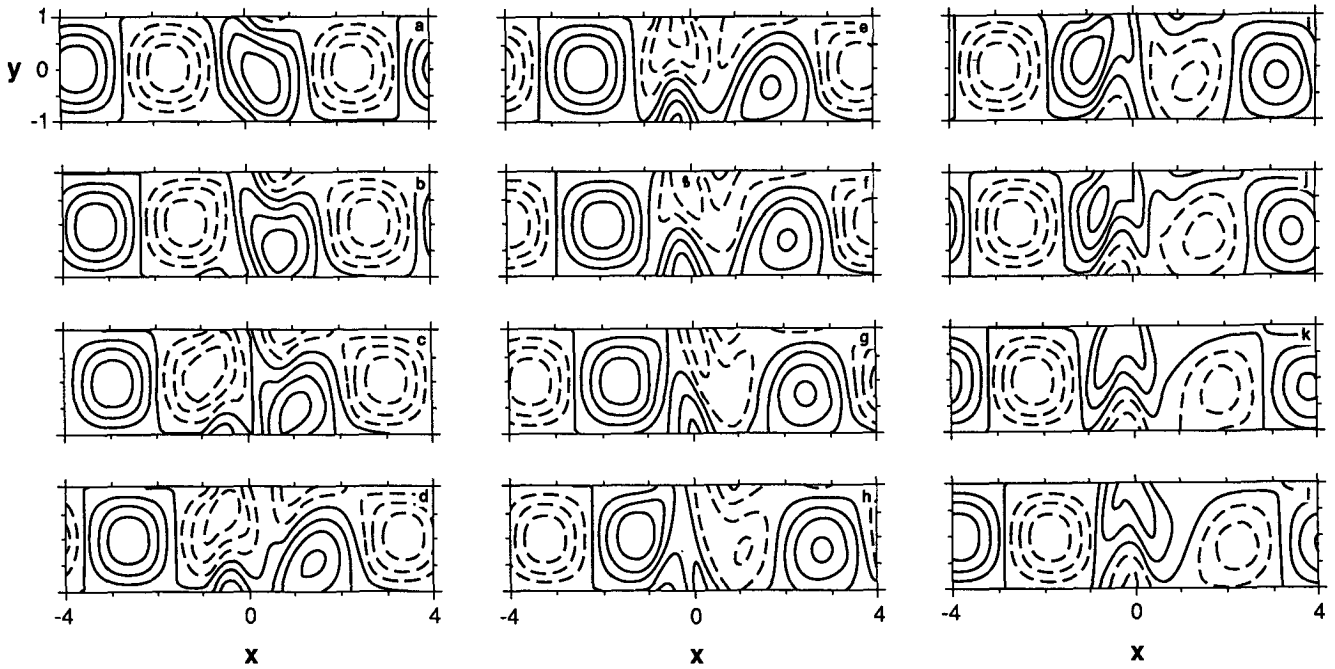

FIG. 4. A contour plot in the x–y plane of the surface pressure field every 6 h for the basic experiment. The domain is $|x| < 4000$ km, $|y| < 1000$ km. The contour interval is one-fourth the maximum at each time. Panels (d), (h), and (l) correspond to hour 0 of day 1, 2, and 3, respectively.

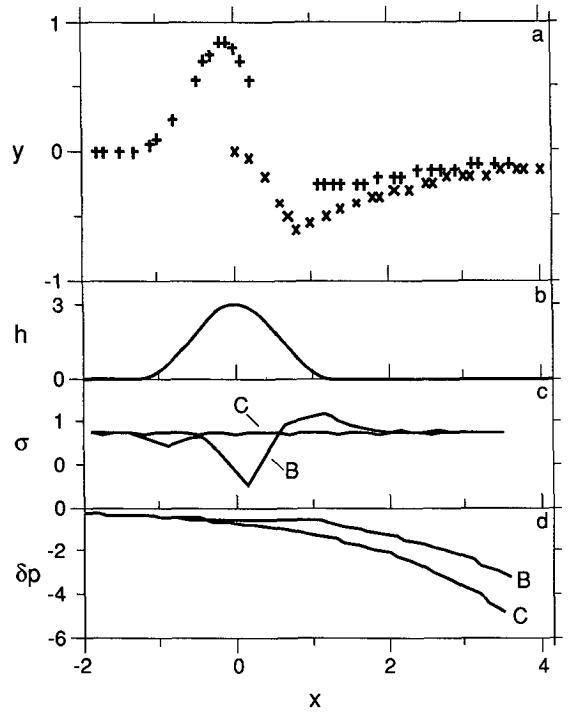

FIG. 5. (a) Loci of points describing the position in the x–y plane of the surface low (+) and high (×) during the basic experiment, (b) the mountain profile, h, in kilometers, (c) the growth rate (day^{-1}) of the surface low for the basic experiment (B) and control (C), and (d) the pressure anomaly δp (10 mb) of the surface low as a function of position x in 1000 km.

mountain, there tends to be adiabatic cooling as well as the squashing of planetary vorticity. These processes tend to produce a cold anticyclonic anomaly that, by the hydrostatic and geostrophic relations, decreases with height. Similarly, regions of descending flow tend to generate shallow warm cyclonic motions. In Fig. 7, this interaction of the primary cyclone wave (denoted by the heavy solid circles) with the mountain (large

TABLE 2. Location and strength of surface low as a function of time.

	t		x	y	δp
(Day)	(h)	(min)	(km)	(km)	(mb)
1	16	00	0	850	−5.73
		30	100	700	−5.67
	17	00	100	700	−5.65
		30	100	700	−5.62
	18	00	100	700	−5.58
		30	100	700	−5.52
	19	00	100	750	−5.44
		30	200	550	−5.41
	20	00	200	550	−5.38
		30	200	550	−5.33
	21	00	200	550	−5.26
		30	300	550	−5.24
	22	00	1000	−250	−5.30
		30	1000	−300	−5.45
	23	00	1000	−300	−5.60
		30	1000	−300	−5.73
2	0	00	1100	−250	−5.88

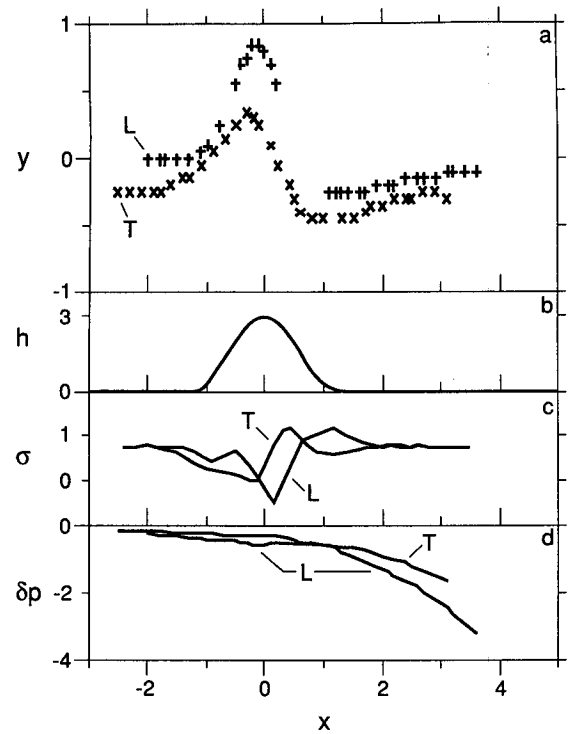

FIG. 6. Position (a), growth rate (c), and pressure anomaly (d) for the surface low (L) and midlevel trough (T). (b) The mountain profile. The points of the midlevel trough in (a) have been displaced southward 250 km for clarity.

inverted carets) produces topographic eddies (thin solid ovals). The oval shape of the topographic eddy is a combination of the elongated meridional extent of the incident wave and the narrow zonal gradient of the mountain slope.

Figure 7a depicts the situation shortly after the initial time of the model simulation. The surface anticyclone generates a quadrople of topographic eddies. Superposition of the two fields yields a NW–SE distortion of the anticyclone consistent with Fig. 4a. As the primary anticyclone moves to the foot of the mountain (Fig. 7b), two dipoles are generated by the system of up- and downslope motions. The total field yields the southeast-high and northeast-low pattern over the mountain (Fig. 4c) as well as the troughing in advance of the surface low. The next situation (Fig. 7c) with the primary low over the mountain is comparable to that of the simulation in Fig. 4e.

This description can be refined in two ways. First, note that the schematics in Fig. 7 only depict the initial generation of the topographic eddies. Once generated, these eddies will be advected downstream by the mean shear flow and will be modified by subsequent thermal advection and vortex stretching. Mathematically, an initial packet of these eddies consists primarily of a sum of growing and decaying Eady waves and neutral, bottom-trapped, Eady edge waves. The latter waves

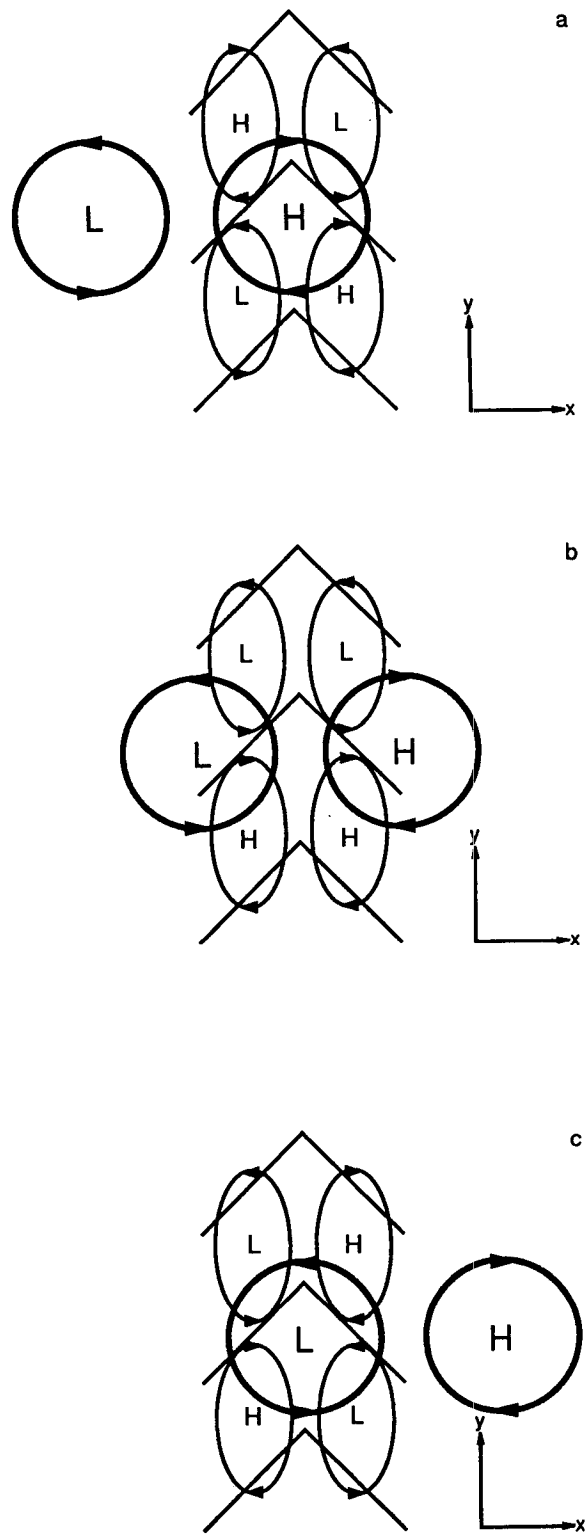

FIG. 7. Schematic diagram describing the interaction of the primary wave (heavy solid circles) with the mountain (large inverted carets) to produce topographic eddies (solid ovals). Panels (a), (b), and (c) refer to times $kc_r t = 0$, $\pi/2$, and π, which refer to the primary low being upstream of, at the base of, and at the top of the mountain ridge, respectively.

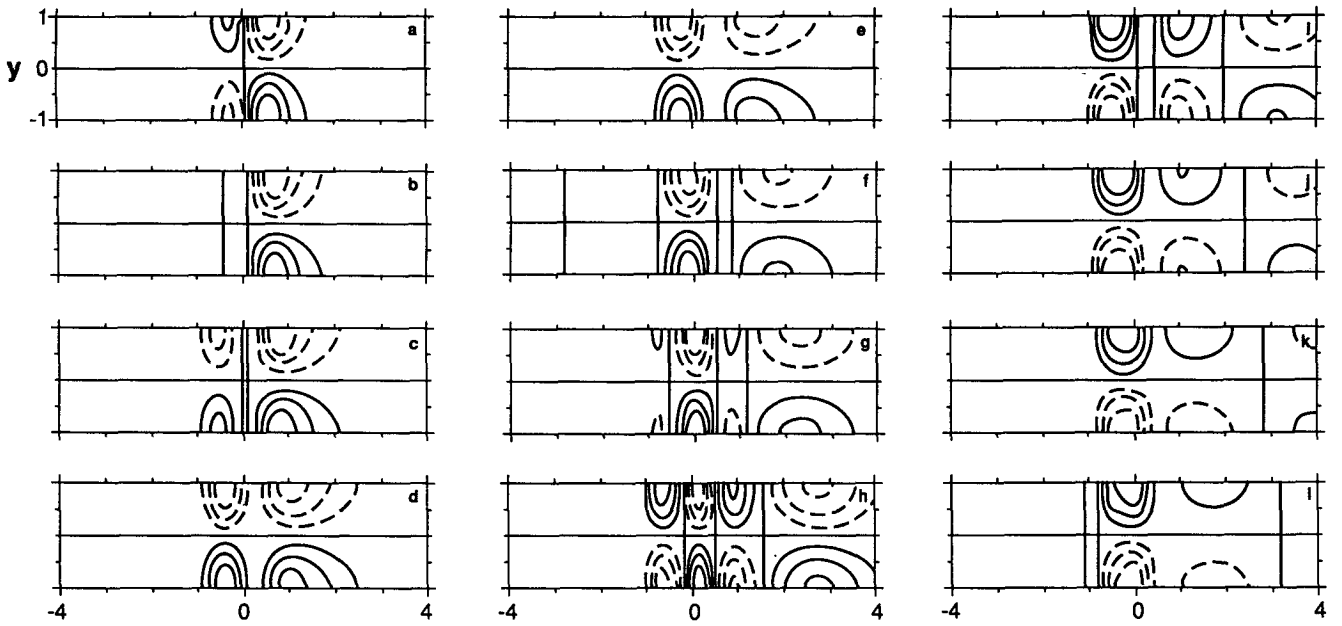

FIG. 8. Similar to Fig. 4 but for the sinuous component of the solution, ϕ_s.

have phase speeds given by the lower curve in Fig. 3. Figure 8 plots the evolution of the surface pressure field associated with the sinuous flow component only. This field displays many of the features suggested by Fig. 7. For example, Figs. 8a, 8c, and 8e approximately correspond to Figs. 7a–c. Clearly evident in Fig. 8, but lacking in Fig. 7, is the downstream dispersion of the modes. Consistent with Fig. 3, the longer wavelength disturbances propagate downstream faster. The dispersive nature of the topographic eddies, their generation at the lower boundary, their slower phase speed, and their weaker structure aloft (not shown) all suggest that the sinuous eddies are primarily neutral, bottom-trapped, Eady edge waves.

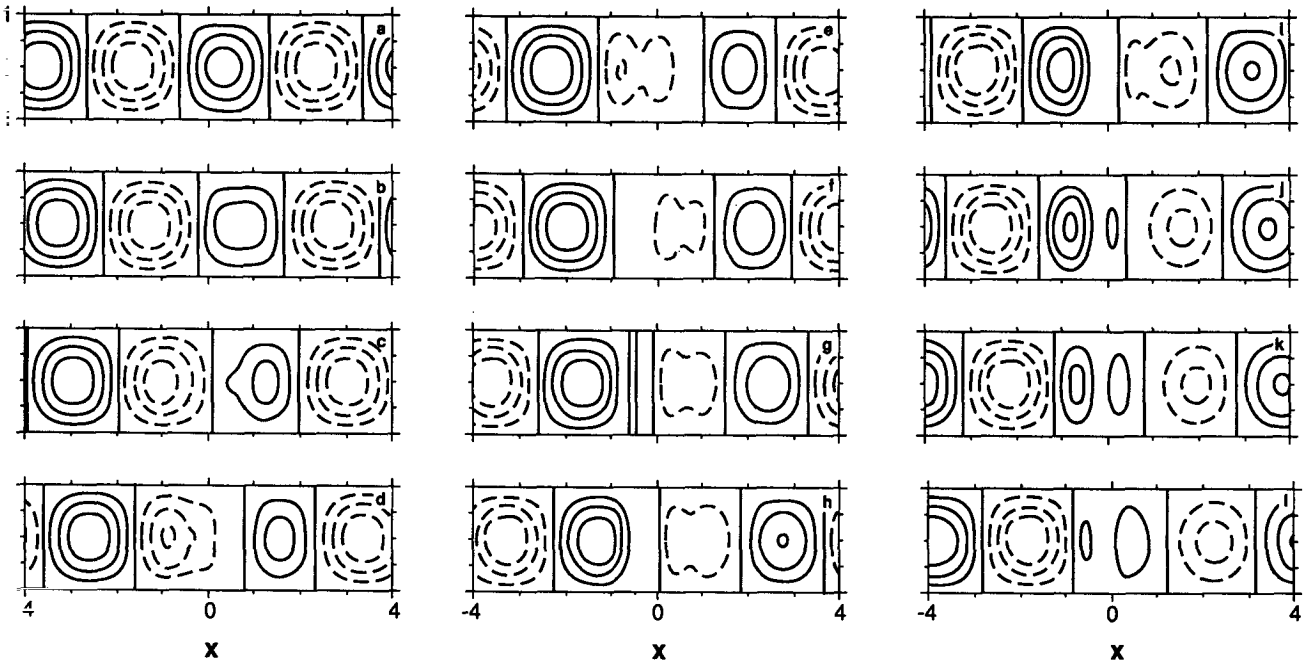

FIG. 9. Similar to Fig. 4 but for the cosinuous component of the solution, ϕ_c.

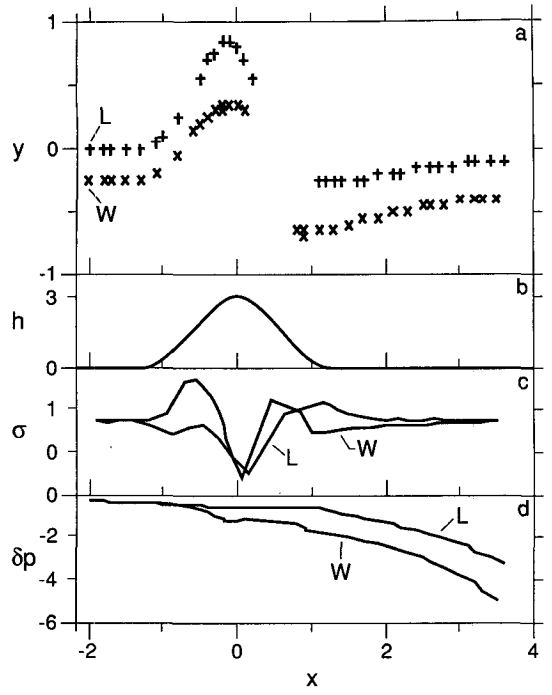

FIG. 10. Position (a), growth rate (c), and pressure anomaly (d) for the surface low with (L) and without (W) the orographic influence on the cosinuous solution component. The W points in (a) are displaced southward 250 km for clarity.

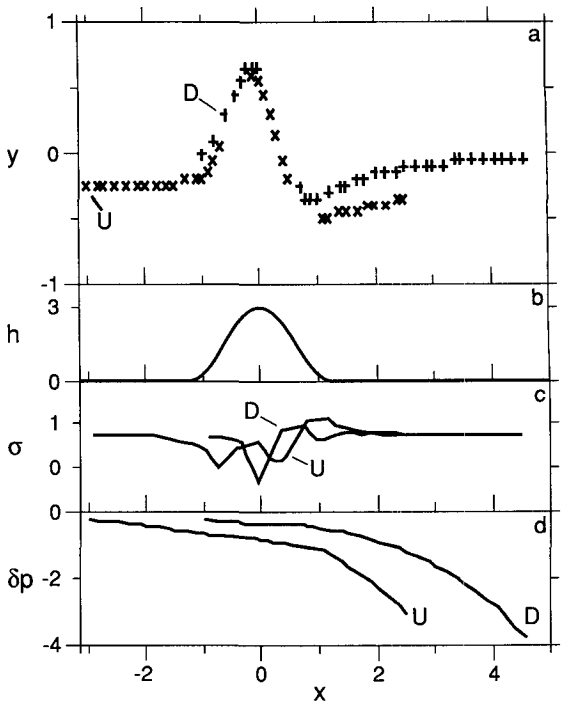

FIG. 12. Position (a), growth rate (c), and pressure anomaly (d) for the surface low initially displaced 1000 km upstream (U) and downstream (D) of the mountain (b). The U points in (a) are displaced southward 250 km for clarity.

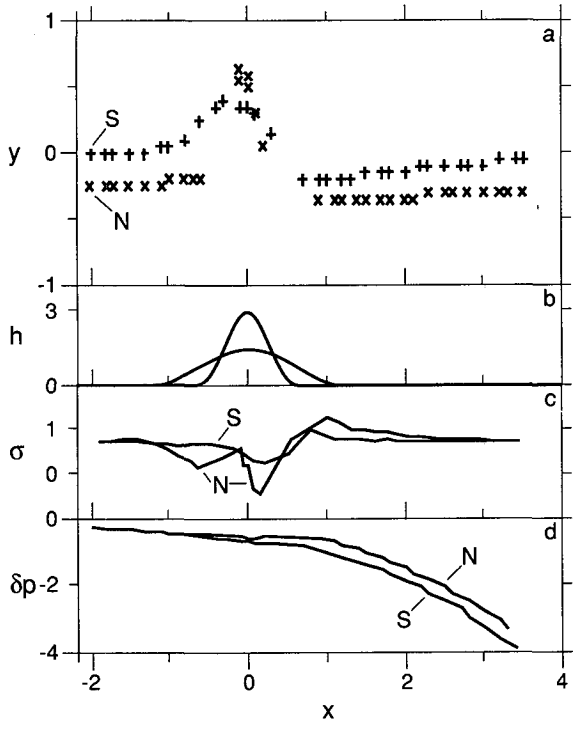

FIG. 11. Position (a), growth rate (c), and pressure anomaly (d) of the surface low for a lower mountain (S) and a narrower mountain (N). Panel (c) depicts the mountain profile in each case. The N points in (a) are displaced southward 250 km for clarity.

The second refinement follows from the observation that the topographic eddies will also interact with the topography. For example, the sinuous lee eddies of Fig. 7c combine to give upslope flow that would lead to the production of a cosinuous anticyclone pair (not shown). This cosinuous eddy pair has the correct phasing to weaken the primary low. Its relatively large horizontal extent ensures it will have a spectral component with a zonal wavelength comparable to that of the primary wave.

This mechanism is crucial for the permanent weakening of the primary wave. Figure 9 clearly depicts this process by isolating on the cosinuous flow component. Note, for example, that the cosinuous low in panels (e) and (f) is reduced in amplitude by an anticyclonic dipole pair.

The importance of this mechanism is further emphasized in Fig. 10, which compares the cyclogenesis with and without the orographic influence by the sinuous component on the cosinuous. The solution without the feedback displays a smaller poleward displacement with greater deepening upstream. Downstream the low appears farther to the south than that in the control (compare Figs. 5d and 10d), but has a similar amplitude. It should be noted that, by their orthogonality, the sinuous component can only distort the low of the primary wave spatially, while the orographically generated contribution to the cosinuous component can alter its strength.

These findings suggest that the net weakening of the primary cyclone results from the orographic generation of an unstable Eady wave with the opposite phase. This conclusion is consistent with Figs. 5c and 5d, which together show that although the low has been weakened by its passage over the mountain, its growth rate remains unaltered.

4. Sensitivity experiments

The model was run for a variety of cases in order to assess the sensitivity of the results of the basic experiment to the parameter settings of Table 1. In general, the findings are consistent with the simple qualitative model described above. Here the results of these experiments are briefly summarized.

a. Orography

Figure 11 summarizes the results for lower and narrower mountains. A lower mountain (h_0 = 1.5 km) produces a smaller (by about a factor of 2) meridional displacement of the low as it crosses the ridge. The low experiences similar but weaker periods of reduced, then amplified, growth before appearing stronger downstream than the higher mountain case (h_0 = 3.0 km). The cyclolytic effect of the mountain is consistent with Fig. 5. Most importantly, the low appears to move more

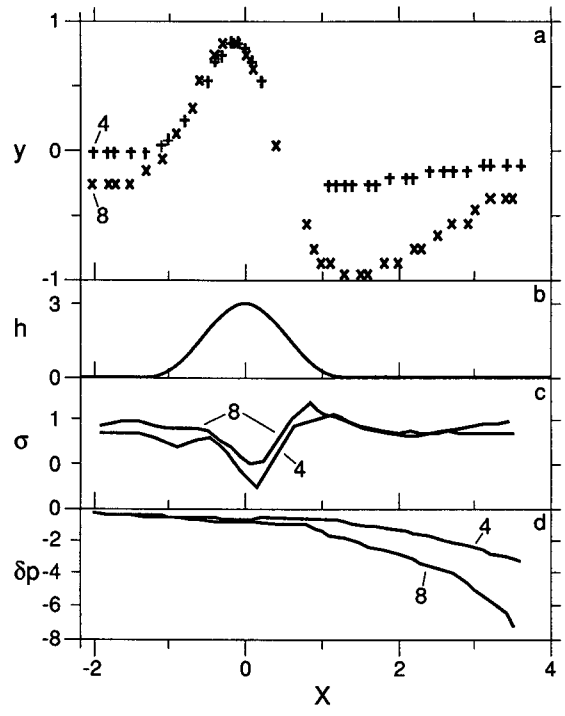

FIG. 14. Position (a), growth rate (c), and magnitude (d) of the surface low for a primary wave of meridional wavelength 4000 (4) and 8000 (8) km, respectively. Panel (b) depicts the mountain profile. The eight points in (c) are displaced southward 250 km for clarity.

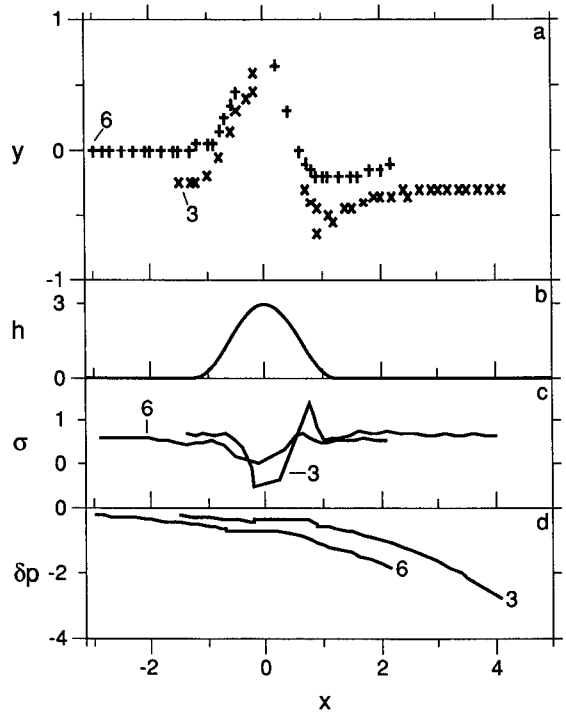

FIG. 13. Position (a), growth rate (c), and pressure anomaly (d) of the surface low for a primary wave of zonal wavelength 6000 (6) and 3000 (3) km, respectively. Panel (b) depicts the mountain profile. The three points in (a) are displaced southward 250 km for clarity.

or less continuously across the ridge without the abrupt jump in position displayed in the benchmark case.

Reducing the mountain wavelength from 4000 to 2000 km produces a narrower mountain with steeper slopes. In this case, the poleward deflection of the low is 100 km greater, while equatorward it is 200 km less than the benchmark. In this case, the low abruptly jumps poleward when it reaches the upstream foothills before its equatorward jump on the lee side. While the extrema in the growth curve are larger, this low is only slightly stronger just downstream of the mountain than that of the basic experiment.

b. Phase of initial conditions

In the basic experiment, the surface high pressure cell is located directly over the ridge top at $x = 0$. Dis-

TABLE 3. Effect of friction over the mountain and variable Coriolis parameter on the location, time, and magnitude of the maximum poleward and equatorward displacement of the surface low.

Case	Poleward displacement (x, y, t, δp) (km, km, time step, mb)	Equatorward displacement (x, y, t, δp) (km, km, time step, mb)
Basic experiment	(−200, 850, 67, −5.8)	(1000, −300, 94, −5.5)
with friction	(−200, 750, 69, −4.1)	(800, −250, 88, −3.7)
with β	(−200, 900, 72, −6.1)	(1200, −300, 123, −8.2)

placing the initial primary wave upstream one-quarter wavelength (see Fig. 12) leads to a larger, more abrupt poleward displacement of the low followed by a smaller, more gradual equatorward one. Conversely, a downstream shift in the initial conditions reduces the poleward displacement of the low on the upslope but slightly increases the equatorward displacement on the downslope. These differences reflect the influence of the dispersive topographic eddies generated in advance of the approaching low. In all cases, however, an upstream reduction in growth rate is followed by a downstream increase.

c. *Structure of the primary wave*

Figures 13 and 14 document the effect of varying the zonal and meridional wavelength on the flow, respectively. Figure 13 indicates that a zonally shorter wave experiences a greater interaction with the mountain. This behavior is qualitatively consistent with the effect of a shift in initial position of the surface low as depicted in Fig. 12. In contrast, Fig. 14 shows that the mountain distorts the meridionally wider wave more. This later result appears at odds with the lower boundary condition (2.5) for which the rising motion increases inversely with the meridional wavelength. Indeed, the orography has no influence for $l = 0$. However, the initial generation of the orographic eddies are centered one-quarter wavelength poleward of the x axis, implying larger meridional displacements. Note that the overall displacement, normalized as a percentage of the meridional wavelength, is less for the wider wave.

d. *Friction*

Newton (1956) suggests that differential friction in the lee would help intensify the low. Thus, an Ekman pumping contribution of the form

$$w_E(x, y, 0, t) = \sqrt{K/2f}\,\nabla^2\phi H[h(x)] \quad (4.1)$$

is added to the lower boundary condition (2.5). Here $K = 10\ \mathrm{m^2\ s^{-1}}$ is the coefficient of eddy viscosity. The factor $H[h(x)]$ in (4.1), where H is the Heaviside step function, ensures that pumping is present only over the mountain. The results (see Table 3) indicate that the friction has a weak cyclolytic effect.

e. *β effect*

It is straightforward to include the effect of a variable Coriolis parameter. The results for $\beta = 1.7 \times 10^{-11}\ \mathrm{m^{-1}\ s^{-1}}$ (Table 3) suggest a slight weakening and deceleration of the low. This behavior is consistent with the stabilizing effect of the beta parameter on the primary wave and its tendency to produce westward propagation. Note that no Rossby lee trough is generated in this case since the surface wind is identically zero.

5. Conclusion

A simple model of cyclogenesis in the lee of the Rockies has been presented. The model design reflects the hypothesis that the cyclogenesis results fundamentally from the interaction of a growing baroclinic wave with the orography of the region. The model's ability to simulate the salient features of the cyclogenesis, as described in section 3, lends support to this hypothesis. In addition, the model successfully addresses the shortcomings of earlier studies noted in the Introduction.

That the model succeeds without a mean surface flow suggests that a mean flow–orography interaction is of secondary importance. As noted by Hayes et al. (1987), a surface flow would generate a high pressure ridge on the mountain that would further mask the movement of the low over the mountain. In addition, a Rossby lee trough would, by supposition, lead to some apparent deepening downstream.

It should be noted that both the primary wave and the topographically induced eddies are modal in their structure. Thus, a nonmodal formulation of lee cyclogenesis, while it would undoubtedly add greater variety to the simulation, does not appear to be a fundamental

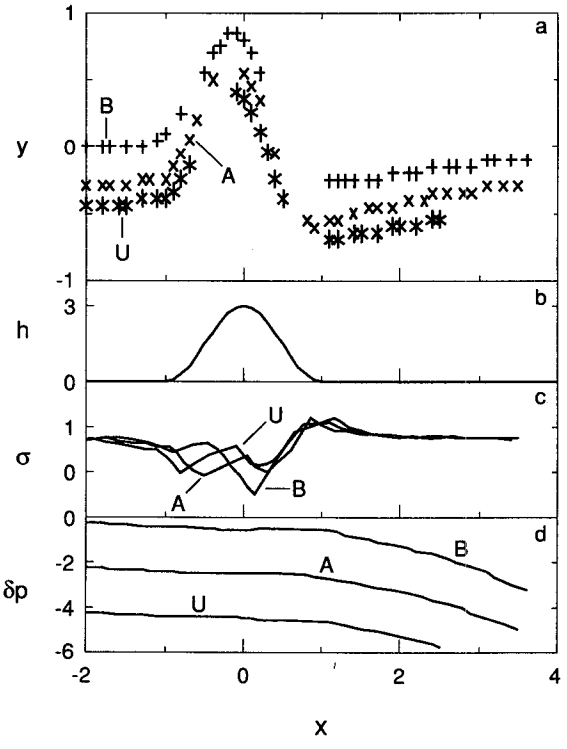

FIG. 15. Position (a), growth rate (c), and magnitude (d) of the surface low for the basic experiment (B), for the low initially displaced 1000 km upstream (U), and for the asymptotic (i.e., normal-mode) solution (A). Panel (b) depicts the mountain profile. The A (U) points in (a) are displaced 250 (500) km southward and reduced by 20 (40) mb in (d) for clarity.

requirement. Note also that the uniform potential vorticity assumption used here precludes the excitation of the continuous spectrum.

A crucial simplification of the present model is the assumed meridional structure of a single sinuous and cosinous mode. This structure, which may be interpreted as the lowest-order spectral representation of the baroclinic wave–orography interaction, greatly restricts the form of the topographic response. Efforts should be made to relax this constraint.

It is worthwhile to compare the present model and its findings with that of Buzzi et al. (1987; henceforth BSTT). The basic hypothesis that lee cyclogenesis is the result of the interaction of a growing baroclinic wave with the orography is the same for each study. However, the methodologies are different but complementary.

BSTT use a normal-mode approach to interpret lee cyclogenesis, with particular emphasis on the most unstable mode in the presence of orography. According to linear theory, this single mode will eventually dominate the solution (excluding the contribution from the continuous spectrum, if any). Evidence that such dominance holds in a nonlinear formulation of their model and in the statistical behavior of a climatological dataset of the real atmosphere has been presented by Buzzi et al. (1990) and by Buzzi and Tosi (1989), respectively. Such evidence provides compelling support for the basic hypothesis of the origin of lee cyclogenesis.

The present model, in contrast, uses an initial value approach to the problem of lee cyclogenesis and examines the transient behavior of a baroclinic wave–orography interaction. Thus, lee cyclogenesis is treated as a forecasting problem, with the goal being the prediction of the short-term evolution of a particular initial condition. An analysis using the single most unstable mode is inadequate in this regard since the complete set of normal modes (with a continuous spectrum, if any) is required to resolve a general initial condition. Here we have chosen an initial condition comprising a single normal mode in the absence of topography. This choice is not arbitrary but reflects synoptic experience as discussed in the Introduction. The temporal evolution of the flow and its interaction with the topography has been discussed, employing the normal modes of the model in the absence of topography: specifically, the generation of topographic eddies as the result of the scattering of an incident baroclinic wave by a meridional mountain ridge and their subsequent evolution. This discussion is distinct from that of Trevisan and Giostra (1990; section 2), who interpret lee cyclogenesis in terms of the effect of a zonal mountain ridge on the potential vorticity dynamics of the most unstable normal mode.

The short-term integrations presented here represent a transient phase in which the initial flow of a normal mode without topography starts to evolve toward the normal mode with topography. This behavior follows, since the normal mode with topography will be the asymptotically dominant feature in a linear analysis. This dominance can only be achieved in a meridional channel that is zonally periodic. We note that while the integration of Trevisan and Giostra (1990) require 20 days for the normal mode to become dominant, the early stages of their solution display features in agreement with the topographic normal mode and with observed cyclogenesis over the Alps.

Figure 15 provides a comparison of the initial value approach with the most unstable normal mode. Here the normal mode is determined numerically by a 36-day integration of the model with the benchmark conditions of section 3. Figure 15 displays this asymptotically dominant mode over the last 4 days of the integration. At day 32 a low is centered 2000 km upstream of the mountain top. The pressure field is scaled to 2.5 mb at day 32 in Fig. 15 for comparison with the initial value solution. Inspection of Fig. 15 indicates that the asymptotic solution displays virtually the same features as those of the benchmark calculation. Slight differences in the growth rates can be attributed to the preconditioning of the flow by the distortion of the leading high pressure cell of the baroclinic wave [compare the asymptotic curve, A, in Fig. 15c with the curve U for the initial value problem with the low displaced 1000 km upstream (see section 4b)]. Despite these differences, the evolution of the surface pressure field is the same. Plots of the surface pressure (not shown) are similar to those in Fig. 4, but with a more disturbed anticyclone over the mountain initially and a reduction in the lee troughing.

These findings suggest that the asymptotic normal-mode solution in the presence of topography consists of the normal mode in the absence of topography and the topographically generated eddies. As noted in section 3b, the sinuous eddies are primarily neutral, bottom-trapped, Eady edge waves that disperse downstream. The interaction of the incident growing baroclinic mode with the mountain constantly generates new edge waves. The most recently generated eddies will be dominant, however, since the incident unstable wave continues to grow indefinitely in this linear model. For example, the time between consecutive passes of an incident low pressure field corresponds to about four e-folding times.

Figure 15c also shows that the mountain does not reduce the growth rate globally. This inconsistency with the normal-mode studies of Pierrehumbert (1986) and Speranza et al. (1985) may arise from the use here of a meridionally uniform mountain profile. Nonetheless, there is a net cyclolytic impact by the topography on the incident low (Fig. 15d). This cyclolysis is interpreted in section 3b as the result of the generation by the sinuous topographic eddies of a cosinuous unstable Eady wave with a phase opposite to that of the incident wave.

Both initial-value and normal-mode approaches provide good simulations of various signatures of lee cyclogenesis, including distortion of the storm track, the formation of an antecedent lee trough, the weakening of the low, and its reemergence on the lee side. Buzzi and Tosi (1989) report a relative maximum in the standard deviation of the high-pass filtered geopotential height in the lee of the Rockies that agrees with the horizontal structure of the amplitude of their most unstable mode. This feature is not evident in the present results. In addition, the reintensification occurs relatively far downstream. Possible explanations for these discrepancies with BSTT may reside in the present use of an infinite ridge mountain in the Eady model rather than their elongated but isolated topography in a two-layer model with a weak, horizontally sheared, basic-state zonal wind profile. Resolution of these issues remains for future research.

Acknowledgments. I thank my colleagues Professors T. N. Carlson and J. H. E. Clark for their helpful discussions on lee cyclogenesis. Financial support, in part, was provided by the National Science Foundation (NSF) under NSF Grant ATM-8813315. Computer facilities were provided by the National Center for Atmospheric Research, which is sponsored by NSF.

REFERENCES

Bannon, P. R., 1991: Aspects of rotating shear flow over a mountain ridge. *J. Atmos. Sci.*, **48,** 211–216.

——, and J. A. Zehnder, 1989: Baroclinic flow over a mountain ridge. *J. Atmos. Sci.*, **46,** 703–714.

Buzzi, A., and S. Tibaldi, 1978: Cyclogenesis in the lee of the Alps: A case study. *Quart. J. Roy. Meteor. Soc.*, **104,** 271–287.

——, and A. Speranza, 1986: A theory of deep cyclogenesis in the lee of the Alps. Part II: Effects of finite topographic slope and height. *J. Atmos. Sci.*, **43,** 2826–2837.

——, and E. Tosi, 1989: Statistical behavior of transient eddies near mountains and implications for theories of lee cyclogenesis. *J. Atmos. Sci.*, **46,** 1233–1249.

——, A. Speranza, S. Tibaldi, and E. Tosi, 1987: A unified theory of orographic influences upon cyclogenesis. *Meteor. Atmos. Phys.*, **40,** 91–107.

——, P. Malguzzi, and A. Trevisan, 1990: The statistical properties of the interaction of high-frequency eddies with mountains in a two-layer model. *Tellus,* **42A,** 28–40.

Carlson, T. N., 1961: Lee side frontogenesis in the Rocky Mountains. *Mon. Wea. Rev.*, **89,** 163–172.

——, 1991: *Mid-latitude Weather Systems.* Harper Collins, 501 pp.

Clark, J. H. E., 1990: An observational and theoretical study of Colorado lee cyclogenesis. *J. Atmos. Sci.*, **47,** 1541–1561.

Eady, E. T., 1949: Long waves and cyclone waves. *Tellus,* **1,** 33–52.

Fawcett, E. B., and H. K. Saylor, 1965: A study of the distribution of weather accompanying Colorado cyclogenesis. *Mon. Wea. Rev.*, **93,** 359–367.

Hage, K. D., 1961: On summer cyclogenesis in the lee of the Rocky Mountains. *Bull. Amer. Meteor. Soc.*, **42,** 20–33.

Hayes, J. L., R. T. Williams, and M. A. Rennick, 1987: Lee cyclogenesis. Part I. Analytic studies. *J. Atmos. Sci.*, **44,** 432–442.

Hess, S. L., and H. Wagner, 1948: Atmospheric waves in the northwestern United States. *J. Meteor.*, **5,** 1–19.

McClain, E. P., 1960: Some effects of the western cordillera of North America on cyclonic activity. *J. Meteor.*, **17,** 104–115.

Newton, C. W., 1956: Mechanisms of circulation change during a lee-cyclogenesis. *J. Meteor.*, **13,** 528–539.

Palmén, E., and C. W. Newton, 1969: *Atmospheric Circulation Systems.* Academic Press, 603 pp.

Pedlosky, J., 1987: *Geophysical Fluid Dynamics.* 2d ed. Springer-Verlag, 710 pp.

Petterssen, S., 1956: *Weather Analysis and Forecasting. Vol. 1.* McGraw-Hill, 428 pp.

Pierrehumbert, R. T., 1986: Lee Cyclogenesis. *Mesoscale Meteorology and Forecasting,* P. S. Ray, Ed., Amer. Meteor. Soc., 493–515.

Smith, R. B., 1984: A theory of lee cyclogenesis. *J. Atmos. Sci.*, **41,** 1159–1168.

——, 1986: Further development of a theory of lee cyclogenesis. *J. Atmos. Sci.*, **43,** 1582–1602.

Speranza, A., A. Buzzi, A. Trevisan, and P. Malguzzi, 1985: A theory of deep cyclogenesis in the lee of the Alps. Part I. *J. Atmos. Sci.*, **42,** 1521–1535.

Trevisan, A., and U. Giostra, 1990: Dynamical criteria determining lee cyclogenesis. *J. Atmos. Sci.*, **47,** 2400–2408.